ELSEVIER

Biochimica et Biophysica Acta 1501 (2000) 189–199

BIOCHIMICA ET BIOPHYSICA ACTA

BBA

www.elsevier.com/locate/bba

Detection of pathological molecular alterations in scrapie-infected hamster brain by Fourier transform infrared (FT-IR) spectroscopy

Janina Kneipp *, Peter Lasch, Elizabeth Baldauf, Michael Beekes, Dieter Naumann [1]

PG3, Robert Koch-Institut, Nordufer 20, D-13353 Berlin, Germany

Received 22 December 1999; received in revised form 16 March 2000; accepted 22 March 2000

Abstract

In this report a new approach for the identification of pathological changes in scrapie-infected Syrian hamster brains using Fourier transform infrared microspectroscopy is discussed. Using computer-based pattern recognition techniques and imaging, infrared maps with high structural contrast were obtained. This strategy permitted comparison of spectroscopic data from identical anatomical structures in scrapie-infected and control brains. Consistent alterations in membrane state-of-order, protein composition, carbohydrate and nucleic acid constituents were detected in scrapie-infected tissues. Cluster analysis performed on spectra of homogenized medulla oblongata and pons samples also reliably separated uninfected from infected specimens. This method provides a useful tool not only for the exploration of the disease process but also for the development of rapid diagnostic and screening techniques of transmissible spongiform encephalopathies.

Keywords: Scrapie strain 263K; Transmissible spongiform encephalopathy; Microspectroscopy; Spectral mapping; Cerebellum; Medulla oblongata; Pons

1. Introduction

Transmissible spongiform encephalopathies (TSEs) such as scrapie in sheep, bovine spongiform encephalopathy (BSE) in cattle, or Creutzfeldt–Jakob disease (CJD) in man are infectious neurodegenerative disorders of the central nervous system (CNS). In addition to the uncertainties about the exact biochemical and structural composition of their etiological agent [1,2], the pathogenesis and pathology of TSEs are far from being completely understood. Notwithstanding this lack of knowledge, it can be assumed that any pathological change caused by TSE agents is accompanied by disease-specific compositional and structural modifications at the molecular level. To achieve more insight into the molecular parameters underlying the disease process, we employed Fourier transform infrared (FT-IR) spectroscopy to obtain information about structural changes involved in TSE pathogenesis.

Characteristic frequencies, intensities, and bandwidths in an infrared (IR) spectrum allow the identification of functional groups of molecules and the characterization of conformationally distinct structures in biological molecules [3]. IR spectra of biological specimens such as tissues represent the superposition of all infrared-active vibrational modes of the various molecules present. Thus, IR spectroscopy may provide information about the chemical constit-

* Corresponding author. Fax: +49-30-4547-2606; E-mail: kneippj@rki.de

[1] Also corresponding author. Fax: +49-30-4547-2606. E-mail: naumannd@rki.de

0925-4439/00/$ – see front matter
PII: S0925-4439(00)00021-1

uents (proteins, lipids, nucleic acids, polysaccharides, etc.) of the probed material and their chemical structure. Biological systems are of extreme molecular complexity. Therefore, recent breakthroughs in instrumentation and data processing techniques were required to establish IR spectroscopy as a useful tool in medical research. Meanwhile, biodiagnostic applications of IR spectroscopy have been described for different types of microorganisms [4], body fluids [5], tissues [6–8], and also for the detection of pathologically altered anatomical regions in patients with carcinoma [9], multiple sclerosis [10], pathologies involving foreign inclusions [11], and Alzheimer's disease [12].

In the following, we demonstrate the capability of FT-IR spectroscopy to detect pathological changes in brain specimens from Syrian hamsters infected with scrapie strain 263K. To our knowledge, this is the first report on an in situ FT-IR spectroscopic examination of TSE-infected brain tissue. In a pilot study, we used FT-IR microspectroscopy for a detailed comparison of spectra from distinct cerebellar areas. This approach combined sensitivity and structural specificity of FT-IR spectroscopy with the spatial resolution of conventional microscopy and revealed specific spectral differences between the cerebellar layers of diseased and non-infected animals. As demonstrated in a follow-up study, these findings were not restricted to tissue sections but could also be observed for intact tissue pieces and homogenized specimens from other CNS regions. The application of cluster analysis to FT-IR spectra of homogenized pons and medulla oblongata samples permitted a rapid and reliable discrimination between scrapie-infected and uninfected brain material.

2. Materials and methods

2.1. Sample preparation

Brains were taken from outbred female Syrian hamsters (*Mesocricetus auratus*) in the terminal stage of disease (S) after infection with scrapie strain 263K and from non-infected (N) controls. Pairs of animals were age-matched. For the IR mapping experiments brains were frozen at −70°C. Mid-sagittal cryo-sections of 6 μm and 10 μm were prepared and thaw-mounted on IR-transparent BaF_2 slides. These samples required no further fixation and were kept in a dry environment at room temperature. To analyze fully hydrated tissue samples, small pieces of native medulla oblongata and pons material were placed in a removable FT-IR cell with CaF_2 windows and 8 μm path length. Alternatively, adequate amounts of tissue material (70–120 mg) were homogenized in water (10 μl H_2O/mg of tissue) by pottering for 30 s. Aliquots of 35 μl of the tissue suspensions were transferred to a ZnSe sample holder and dried to a transparent film under moderate vacuum (2.5–7.5 kPa) [13]. IR mapping was performed on brain samples from two intraperitoneally infected S animals and three N hamsters. Medulla and pons specimens were obtained from 10 intracerebrally infected and 10 control hamsters. All animal experiments were carried out in accordance with the German and European legal and ethical regulations. They were notified to and approved and surveyed by the authorities for animal protection and control of animal experiments.

2.2. IR data collection

We used an IR microscope (IRscope I) coupled to an IFS28B FT-IR spectrometer (both Bruker, Germany) to map the tissue sections. The microscope was equipped with a computer-controlled x/y stage which permitted spectral sampling of the tissue in defined steps within a rectangular area. A grid of pixel coordinates within the tissue section was defined and IR spectra were collected from each of the points in the grid. Spectra were taken in steps of 50 μm in both the x and the y direction and an aperture diameter of 60 μm. In this way, IR data completely covering the chosen tissue area could be obtained. IR spectra were collected in transmission/absorption from 4000 to 700 cm^{-1} with a spectral resolution of 6 cm^{-1} using an Hg-Cd-Te detector. Twenty-two scans were coadded per pixel spectrum. Signal-to-noise ratios (S/N) were determined from original spectra (using the signal intensities at 1655 cm^{-1} and at 1238 cm^{-1}, respectively) and noise spectra collected through the sample. S/N ratios of about 1000 and 600 were calculated for the amide I region and the spectral region from 1300 to 1000 cm^{-1},

respectively. The microscope, which was hermetically sealed using a specially designed box, and the spectrometer were purged with dry air to reduce spectral contributions from water vapor and CO_2 [9]. IR spectra from the tissue pieces and homogenized samples were also collected in transmission/absorption at a nominal resolution of 4 cm^{-1}. An IFS66 FT-IR spectrometer (Bruker, Germany) was used to measure the hydrated pieces. The homogenized and dried samples were probed with an IFS25B FT-IR spectrometer (Bruker, Germany). Both spectrometers were equipped with a DTGS (deuterated triglycine sulfate) detector.

2.3. IR data evaluation

Analysis of spectral data was carried out using the OPUS 3.0 data collection software package (Bruker, Germany). All interferograms were Fourier-transformed applying a Happ–Genzel apodization function and zero-filled. Analysis of IR mapping data sets was done with a macro interpreter integrated in OPUS 3.0. The spectra were tested for absorption of water vapor using the peak intensities at 1792.4 and 1844.6 cm^{-1} as a criterion: spectra with intensities exceeding values of 2×10^{-5} and 3×10^{-5} at 1792.4 and 1844.6 cm^{-1}, respectively, were not included in the data evaluation (peak intensities were calculated from second derivatives). Offset-corrected absorbance spectra whose integral intensity between 1770 and 1100 cm^{-1} (indicator for the thickness of the cryo-sections) was higher than 250 and lower than 30 were excluded from further analysis. Vector-normalized first derivatives of spectra which passed this 'quality test' were used for principal component analysis and subsequent cluster analysis. Multivariate statistical analysis was done using the 'identity' and 'cluster analysis' modules of OPUS 3.0. Subsequent data processing (evaluations, normalization, distance calculations, combination with original spatial information, etc.) was carried out using software developed in our laboratory. Results were stored in a format readable by Origin 5.0 (Microcal Software, Northampton, MA, USA) for image reconstruction. To facilitate comparison of normal and diseased brain spectra, cluster analyses were performed on first derivative spectra using different wavenumber ranges. Spectral distances were calculated as Pearson's correlation coefficient and Ward's algorithm was used for hierarchical clustering. Direct comparison of spectral characteristics was done on second derivatives of average spectra of the discussed spectral classes to increase the S/N ratio. Difference spectra were smoothed using a Savitzky–Golay algorithm. Average values of band frequencies at 3012, 2851, and 2921 cm^{-1} were determined from the peak positions in original pixel spectra and are given with their standard deviations.

3. Results

3.1. Spectral information and molecular structure

Fig. 1 contains two typical brain tissue IR spectra and the second derivative of one of them. They were obtained from stratum moleculare (a layer of gray matter) and substantia alba (white matter), respectively, of a normal brain tissue section. A brain IR spectrum can roughly be separated into three major absorption regions. Between 3050 and 2800 cm^{-1} spectral features are dominated by absorption bands of the asymmetric and symmetric C–H stretching vibrations of $>CH_2$ and $>CH_3$ methylene groups contained in fatty acids in cellular membranes. These vibrations can be used as sensitive monitors of the state-of-order of the membrane lipid matrix [14]. As is known from earlier studies [8,10], the $>CH_2$ stretching – and also the bending vibration at 1468 cm^{-1} – is very prominent in white matter spectra due to the high myelin content of white matter (see Fig. 1). At around 3012 cm^{-1}, absorption due to C–H stretching vibrations of $=$C–H groups in unsaturated fatty acids can be observed. The spectral region between 1800 and 1500 cm^{-1} is shaped mainly by the $>C=O$ stretching absorption band of ester carbonyl (1738 cm^{-1}) and the amide bands of proteins. The amide I band (mainly amide $>C=O$ stretching frequencies of the protein backbones) components observed between 1700 and 1600 cm^{-1} are conformation-sensitive and can be used to discriminate between the protein secondary structures α-helix and β-pleated sheet, a feature which was already employed to investigate Alzheimer's plaques by IR spectroscopy [12]. Coupled N–H bending and C–N stretching vibrations shape the amide II region be-

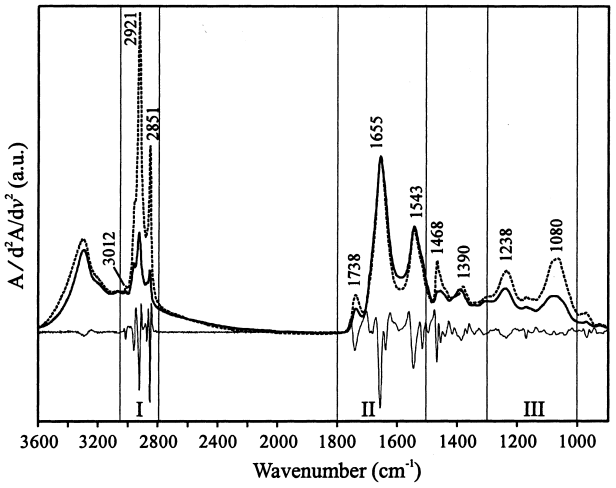

Fig. 1. IR spectra obtained from two cerebellar substructures of an uninfected hamster brain section and the second derivative spectrum of one of the two spectra. The bold line is a spectrum of stratum moleculare (a gray matter substructure) and the thin line is its second derivative. The spectrum of substantia alba (white matter) is shown by the dashed line (given for clarity without its derivative). The three major absorption regions used for spectral comparison in this study are indicated. I: 3050–2800 cm^{-1}, dominated by absorption bands of the asymmetric and symmetric C–H stretching vibrations of $>CH_2$ and $>CH_3$ groups contained in fatty acids in membranes. II: 1800–1500 cm^{-1}. This spectral region is shaped mainly by the $>C=O$ stretching absorption band of ester carbonyl (1738 cm^{-1}), the various conformation-sensitive amide I band (1700–1600 cm^{-1}) and amide II band components (1600–1500 cm^{-1}) of proteins [15]. III: 1300–1000 cm^{-1}. Absorptions in this 'fingerprint region' originate from $P=O$ stretching vibrational modes and characteristic vibrations of DNA/RNA backbone and carbohydrate structures [16].

tween 1600 and 1500 cm^{-1} [15]. Absorptions in the spectral region between 1300 and 1000 cm^{-1} can be associated with $P=O$ double bond stretching modes of phosphate groups carrying compounds and with distinct ring vibrations of carbohydrates [6,16]. Even though a number of absorption bands in this region remain unassigned, the bands around 1240 and 1080 cm^{-1} are known to contain significant contributions from asymmetric and symmetric stretching modes, respectively, of phosphodiester groups (PO_2^-) in nucleic acids [6,16].

3.2. IR imaging of cerebellar sections

Microspectroscopic analysis was carried out on mid-sagittal cryo-sections of five hamster brains in a rectangular area (size varying between 2.5 and 4.5 mm^2 for the different samples) of the cerebellum (Fig. 2A). We applied principal component analysis (PCA) to the spectral data sets to achieve data reduction and to attain classification of spectral patterns (see e.g. [9]). Fig. 2B displays the dendrogram of a hierarchical cluster analysis of one of the five data sets. Spectral distances as input for cluster analysis were based on the first three principal components which comprise 99% of the variance of the data set. Nine distinct classes of spectral patterns, each representing a different tissue structure in the cerebellum, were produced. The classification patterns turned out to be very similar for all analyzed samples.

Spectral distances between each individual spectrum and the center of each of the classes shown in Fig. 2B were calculated as Euclidean distances and utilized to reassemble PCA-based images of the different histological structures (Fig. 2C, see [9]). Each spectral pattern (i.e. tissue structure) was encoded by a different color with color intensity (degree of pat-

→

Fig. 2. IR mapping and imaging procedures applied to the FT-IR data from mid-sagittal cerebellar sections of hamster brains. (A) Cerebellar section (schematic) and methylene blue staining (magnified). The dashed line indicates the tissue area investigated by IR mapping. Staining with methylene blue reveals four cerebellar layers histologically defined by their different cell types and composition. (B) Dendrogram of a hierarchical cluster analysis based on PCA, using the first three principal components (which capture 99% of the variance in the data set) between 1450 and 950 cm^{-1} (approximately 500 data points). The dendrogram displays nine spectral classes within the cerebellum (numbered 1–9). The four major classes correspond to the four histological layers (shown in A). For clarity reasons, only every third spectrum of the complete data set comprising 930 spectra is displayed here. (C) PCA-based IR images (numbered 1–9), each representing a particular structure in the cerebellum, were generated from the pixel spectra of the nine spectral classes (B). Superposition of the nine single maps yielded a complete IR image of the investigated tissue area. We refer to the nine substructures using their cluster number and the name of their cerebellar layer. The substructures stratum moleculare (2), stratum granulosum (4), and substantia alba (8) were used in the following for spectral comparison of scrapie-infected and normal brains (labeled with an asterisk).

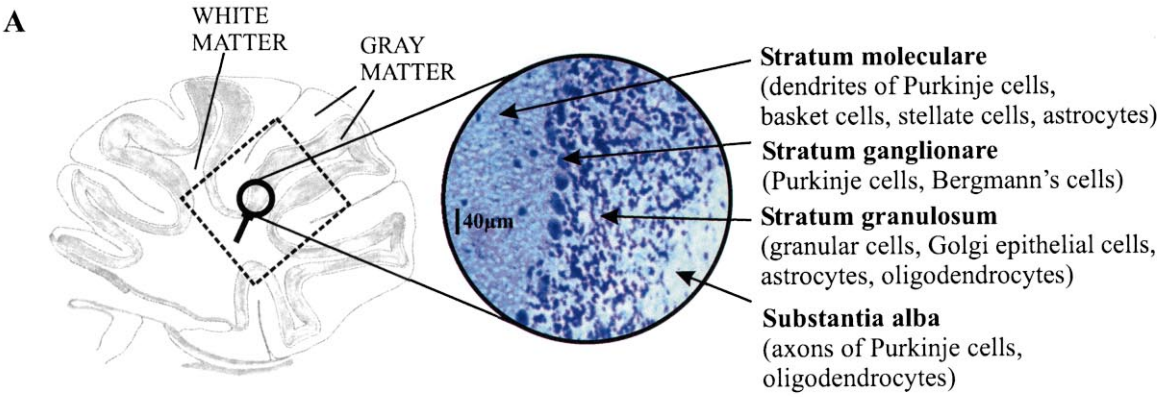
A
WHITE MATTER
GRAY MATTER
40μm
Stratum moleculare
(dendrites of Purkinje cells, basket cells, stellate cells, astrocytes)
Stratum ganglionare
(Purkinje cells, Bergmann's cells)
Stratum granulosum
(granular cells, Golgi epithelial cells, astrocytes, oligodendrocytes)
Substantia alba
(axons of Purkinje cells, oligodendrocytes)

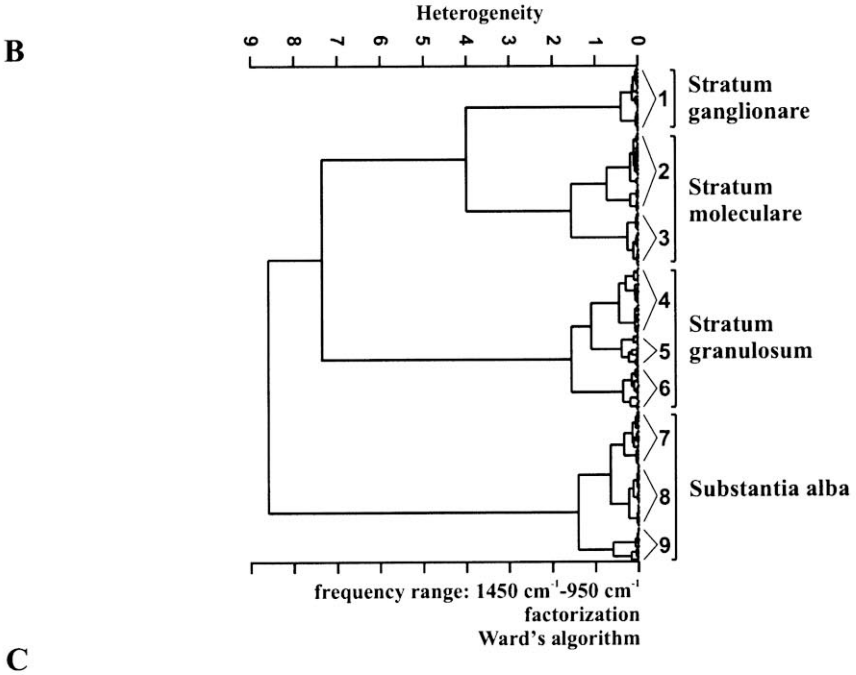
B
Heterogeneity
9 8 7 6 5 4 3 2 1 0
1
2
3
4
5
6
7
8
9
Stratum ganglionare
Stratum moleculare
Stratum granulosum
Substantia alba
frequency range: 1450 cm-1-950 cm-1
factorization
Ward's algorithm

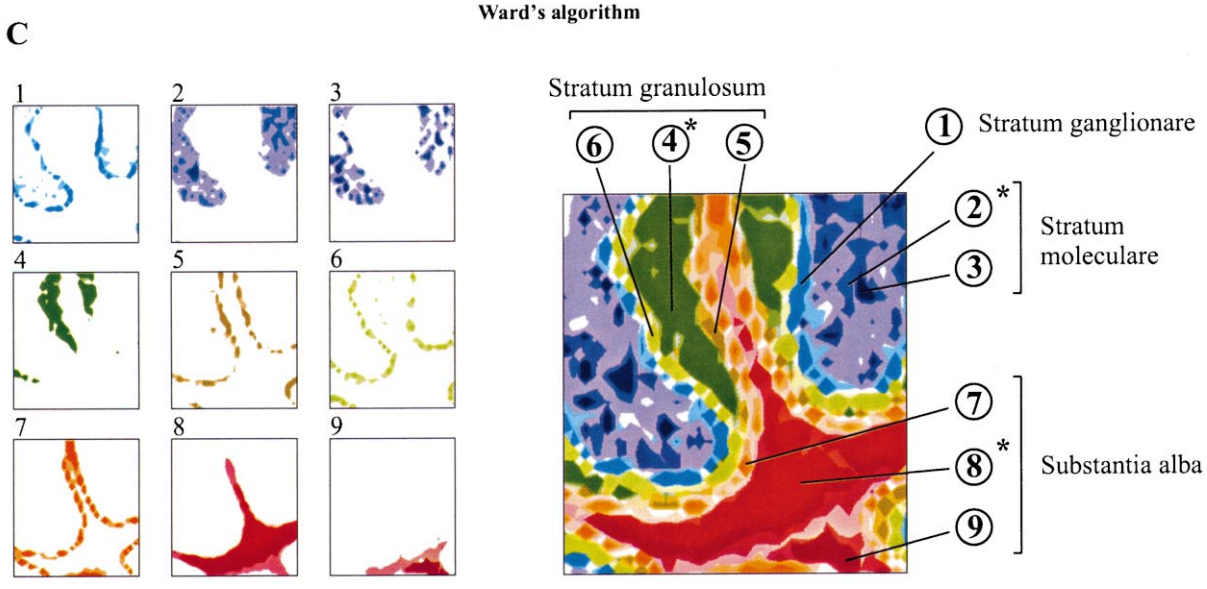
C
1
2
3
4
5
6
7
8
9
Stratum granulosum
Stratum ganglionare
Stratum moleculare
Substantia alba

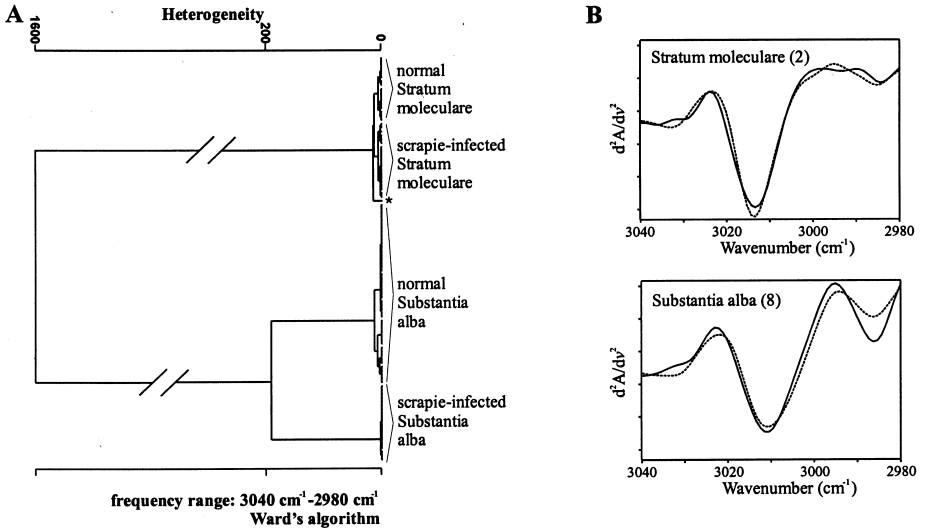

Fig. 3. (A) Cluster analysis of spectra from normal (N) and scrapie-affected (S) stratum moleculare (2) and substantia alba (8) using the spectral range 3040–2980 cm^{-1}. Normalized first derivatives of all original 49 N and 33 S spectra from stratum moleculare (2) and of 45 N and 20 S spectra from substantia alba (8) (extracted from the data set shown in the dendrogram of Fig. 2B) were used for hierarchical clustering. One misclassification (labeled by the asterisk) occurred in the stratum moleculare (2) cluster. (B) Spectra (vector-normalized second derivatives) of the cerebellar structures stratum moleculare (2) and substantia alba (8) of N and S Syrian hamster cerebellar cryo-sections (see also Fig. 2C). The spectra from uninfected (full line) and infected (dashed line) stratum moleculare (2) and substantia alba (8) are averages of 10 individual pixel spectra selected from the center of their spectral classes (see also Fig. 2B). Absorption maxima appear as minima in the second derivatives.

tern expression) with spectral distance being in inverse proportion. The nine images displayed in Fig. 2C give the spatial distribution of the different tissue structures within the cerebellum. Superposition of these nine images yielded a complete 'IR view' of the mapped tissue area (Fig. 2C). Comparison with histological data [17] (Fig. 2A) allowed us to categorize the nine spectral classes into the four histologically defined layers stratum moleculare, stratum ganglionare, stratum granulosum, and substantia alba. Some details about the neuronal composition of these four layers, especially of stratum granulosum (all green structures in Fig. 2C) are known [17], permitting designation of class 4 (small granular cells, glomeruli cerebelli), class 5 (horizontal cells, small granular cells), and class 6 (large and small granular cells, Golgi epithelial cells, horizontal cells). The histological meaning of the remaining IR substructures could not be fully described yet.

3.3. *Structural analysis based on pixel spectra of the IR images*

The assignment of individual spectra of a given spectral map to particular cerebellar substructures enabled us to compare spectra from the same brain structures of scrapie-infected and uninfected hamsters. Single pixel spectra were extracted from the

Table 1
Characteristic absorbance maxima $\bar{\nu}$ (in wavenumbers, cm^{-1}) of the $=C–H$ and $>CH_2$ stretching vibrational bands which are different in the IR spectra of scrapie-infected and normal CNS tissues (average values ± S.D. determined from original spectra)

	$\bar{\nu}$ (cm^{-1})		Assignment of vibration
	N	S	
Stratum moleculare (2)	2852.68 ± 0.07	2852.89 ± 0.05	symmetric $>CH_2$ stretching
	2923.58 ± 0.12	2923.95 ± 0.09	asymmetric $>CH_2$ stretching
Substantia alba (8)	3009.61 ± 0.42	3008.56 ± 0.28	$=C–H$ stretching

subclasses stratum granulosum (4), stratum moleculare (2), and substantia alba (8) (highlighted in Fig. 2C). Cluster analyses on these spectra and subsequent collating of average spectra of the substructures were performed for three spectral regions. Spectra from normal and infected animals displayed a number of differences distributed over the whole spectral range measured. From the cluster analyses we learned that spectral differences between the tissue substructures were much larger than those between N and S. Thus, it was crucial to compare spectra of infected and uninfected material from exactly the same tissue substructure.

The result of a cluster analysis using spectral information between 3040 and 2980 cm^{-1} of normal and infected stratum moleculare (2) and substantia alba (8) is shown in Fig. 3A. As can be seen from this dendrogram, the histological substructures formed two major clusters. Within each of these clusters sub-grouping of N and S tissues was observed. In accordance with the morphological diversity within normal cerebellum, the peak positions of the 3012 cm^{-1} band (=C–H stretching in unsaturated fatty acids) of average spectra of the three chosen structures differed markedly (3009.61 ± 0.41 cm^{-1} in substantia alba (8), and 3013.91 ± 0.15 cm^{-1} and 3012.73 ± 0.35 cm^{-1} in stratum moleculare (2) and stratum granulosum (4), respectively). The differences between normal and infected substantia alba (8) suggested by Fig. 3A include a frequency shift of approximately 1 cm^{-1} in the =C–H stretching band to lower wavenumbers as compared to N spectra (see Table 1 and Fig. 3B) and slight intensity changes. In stratum moleculare (2) a marginal increase in relative intensity and contour of the =C–H stretching band in S spectra can be observed (Fig. 3B). Absorption bands of the $>CH_2$ methylene functional groups in fatty acids (C–H asymmetrical and symmetrical stretching vibrations at 2921 and 2851 cm^{-1}, respectively) were slightly shifted to higher wavenumbers in stratum moleculare (2) of the infected animals (see Table 1). The absorption bands of the C–H asymmetrical and symmetrical stretching vibrations could not be used to compare S and N

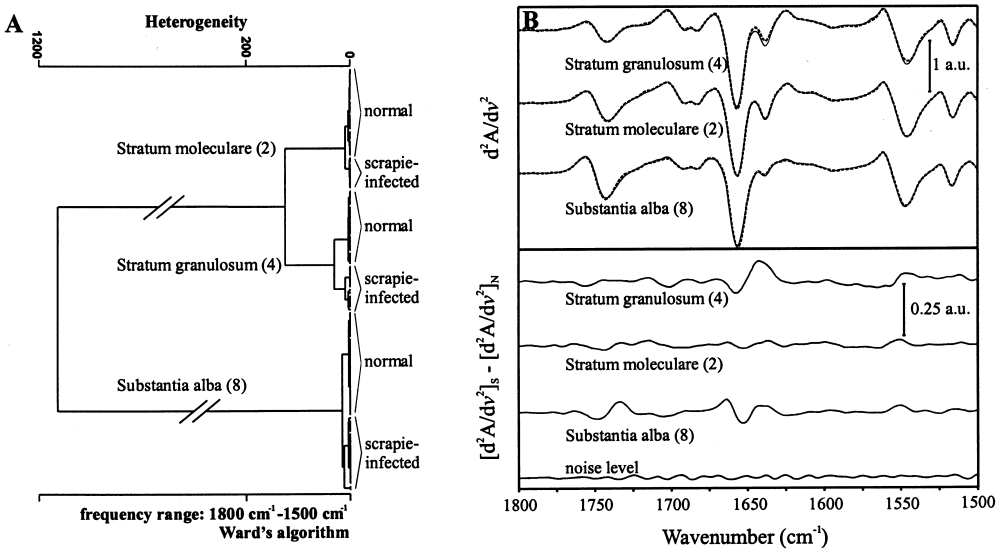

Fig. 4. Comparison of the spectral region between 1800 and 1500 cm^{-1} for three different structures within the cerebellum of N and S Syrian hamster cerebellar cryo-sections (see also Fig. 2C). (A) Hierarchical clustering of normalized first derivatives of 141 original spectra of the three structures stratum moleculare (2), stratum granulosum (4) and substantia alba (8) of N and S brains. The differences between spectra of uninfected and infected samples depend on the morphological structure and are reflected by the different amounts of heterogeneity. There occurred one misclassification (normal classified as infected) in substantia alba (8). (B) Spectra (second derivatives) from uninfected samples are shown as thin lines, those of scrapie-infected samples as dashed lines in the upper panel. The lower panel displays the difference between the second derivatives of S and N spectra (S minus N). All spectra used for comparison are averages of 10 individual pixel spectra selected from the center of their spectral classes (see also Fig. 2B). They are referred to using the cluster number of Fig. 2B and the name of the corresponding cerebellar layer. The second derivative spectra in the upper panels were vector-normalized (note that absorption maxima appear as minima in second derivatives).

white matter spectra, since high absorbance values due to the high myelin content of substantia alba (8) caused detector non-linearity.

The structure-specific variations of the S spectra in the protein amide I and amide II region (1800–1500 cm^{-1}, Fig. 1) are shown in Fig. 4. The varying degree of pathological change in the different layers is reflected by the different degree of heterogeneity between N and S within the three major classes in the dendrogram (Fig. 4A). Between 1675 and 1625 cm^{-1} (amide I) as well as between 1550 and 1500 cm^{-1} (amide II) differences in the line shape and intensities between N and S spectra were observed for stratum granulosum (4) and substantia alba (8) (Fig. 4B). In substantia alba (8) these variations were accompanied by a slight peak shift. In contrast, N and S spectra of stratum moleculare (2) were nearly identical in the range of 1700–1500 cm^{-1} and showed neither frequency shifts nor intensity or bandwidth changes (Fig. 4B).

Additional spectral alterations were located between 1300 and 1000 cm^{-1} (Fig. 5). The cluster analysis (Fig. 5A) showed clear separation between spectra of normal and diseased stratum moleculare (2) and substantia alba (8). In the spectral class stratum granulosum (4), for which separation into N and S was observed in the amide spectral region (see Fig. 4A), there occurred a number of misclassifications over the spectral range from 1300 to 1000 cm^{-1} (Fig. 5A). Band contour changes in this region (Fig. 5B) can be assigned to altered IR absorption of P=O double bonds in phosphate group-carrying compounds, and also of carbohydrates (C–O, C–C and C–O–C stretching vibrations) such as sugars in the backbone of DNA and RNA structures.

3.4. Spectral data from tissue pieces and homogenized samples of medulla and pons

To complement the spatially resolved IR data acquired from a small number of individuals, the preparation technique was simplified in order to scrutinize the spectral characteristics of a larger group of animals. IR spectra were obtained from medulla oblongata and pons preparations (homogenized samples dried to thin films and tissue pieces) from 10 S

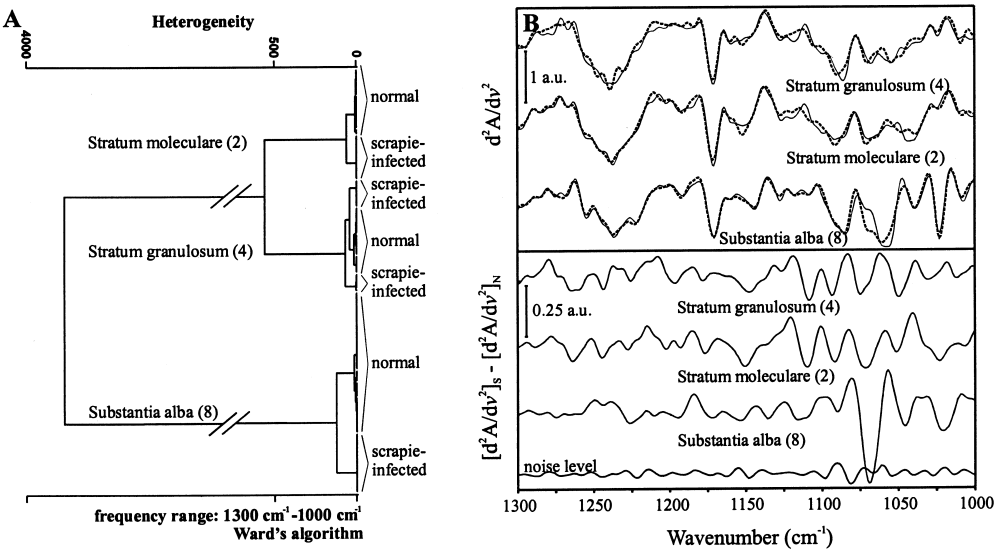

Fig. 5. Comparison of the spectral region between 1300 and 1000 cm^{-1} for three different structures within the cerebellum of N and S Syrian hamster cerebellar cryo-sections (see also Fig. 2C). (A) Hierarchical clustering of normalized first derivatives of 141 original spectra of the three structures stratum moleculare (2), stratum granulosum (4) and substantia alba (8) of normal and scrapie-infected brain. The differences between spectra of uninfected and infected samples depend on the morphological structure and are reflected by the different amounts of heterogeneity. Spectra obtained from stratum granulosum (4) were not clearly divided into N and S, there occurred misclassifications for spectra of this cerebellar structure. (B) Spectra (second derivatives) from uninfected samples are shown as thin lines, those of scrapie-infected samples as dashed lines in the upper panel. The lower panel displays the difference between the second derivatives of S and N spectra (S minus N). See legend of Fig. 4B for details on the spectra.

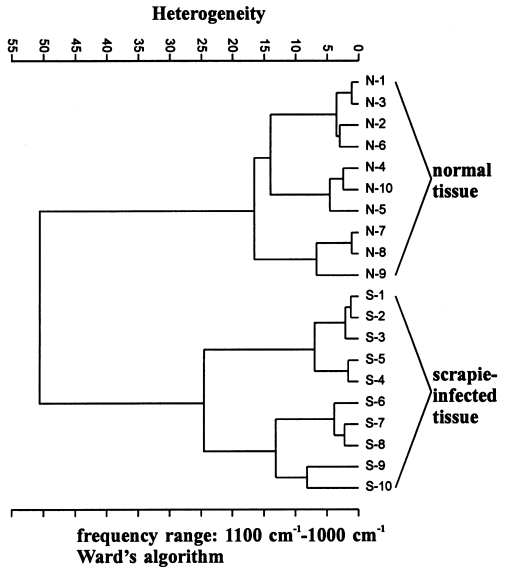

Fig. 6. Dendrogram of a hierarchical cluster analysis (CA) performed on spectra of homogenized pons and medulla oblongata specimens of 20 individuals, 10 scrapie-infected (S-1–10) and 10 uninfected (N-1–10). CA was based on spectral information contained in the spectral range 1100–1000 $cm^{-1}$of normalized second derivative spectra.

and 10 N hamsters. Again, characteristic band contour changes, intensity variations, and band shifts were observed for almost all parts of the S spectra. They were consistent with the spatially resolved observations in the tissue sections. Alterations in S spectra, such as the intensity decrease at 3012 cm^{-1} and the frequency shift at 2851 cm^{-1}, closely resembled those found for white matter of the cerebellum.

The 'fingerprint region' (1300–1000 cm^{-1}), which contains information about nucleic acids, carbohydrates, and phosphorylated lipids and proteins in the tissue, showed most of the changes in S spectra of pons and medulla oblongata. When the spectral data of homogenized pons and medulla oblongata specimens from 20 individuals were subjected to cluster analysis, two clusters were produced, corresponding to infected and uninfected samples, respectively (Fig. 6).

4. Discussion

IR spectroscopy in combination with microscopy yielded spatially resolved information on unstained cerebellar thin sections of brain samples from *Mesocricetus auratus* that allowed the generation of IR maps with high image contrast. The assignment of spectral features to specific anatomical locations was possible using multivariate pattern recognition techniques and permitted the precise collating of IR characteristics of identical regions in scrapie-infected and control hamster brains.

4.1. Pathological molecular changes in scrapie

Frequency shifts of $>CH_2$ methylene and $=C–H$ stretching bands in the S material indicated alterations in the composition and structure of cellular membrane systems. As previously shown for a scrapie mouse model, the majority of membrane lipids remain unaltered in infected brain, except for the level of dolichol which drops dramatically [18]. $>CH_2$ vibrational modes were shifted to higher energies in samples from scrapie hamsters, indicating a diminished state-of-order [19,20] in scrapie-affected cerebral membranes. Cellular membranes are lipid–protein assemblies, and protein composition is also known to be modified during the course of scrapie [21]. It seems conceivable that an altered protein composition of the membranous systems could influence membrane state-of-order via lipid–protein interactions (see e.g. [22]). Changes in the membrane protein composition and/or an increase in relative protein amount would lead to a decreased membrane state-of-order. Excess catabolic activities including lipid peroxidation leading to cross-linking among membrane lipids are known for mitochondrial membranes [23] and could also contribute to the observed decrease in state-of-order. Furthermore, increased α-tocopherol and total ubiquinone levels, which have been described for the mouse model [18], may influence IR absorption. However, these interpretations might remain very hypothetical, since further details about membrane alterations in scrapie pathology are unknown yet.

Variations in IR bands between 1300 and 1000 cm^{-1} indicating changes in the amount of nucleic acids and/or different degrees of phosphorylation of carbohydrates and/or glycoproteins proved to be quite characteristic for the S samples in our study. Even the small spectral region between 1100 and 1000 cm^{-1} provided sufficient information to reliably

distinguish between uninfected and infected tissue (Fig. 6). The exact structural basis of these findings remains to be deciphered and must be addressed in future studies.

One of the most striking molecular features of scrapie and other TSEs is the accumulation of the pathological prion protein PrP^{Sc}, which exhibits a much higher content of β-pleated sheet structure than PrP^{C}, its cellular precursor [24]. In contrast to Alzheimer's disease, where amyloid plaque formation in the brain can be detected by FT-IR spectroscopy based on changes in the amide I band [12], we observed a slight decrease (!) in β-pleated sheet content in scrapie-infected tissue (Fig. 4A). At first glance, this finding appears surprising, however, the amount of PrP^{Sc} in the brain of terminally ill hamsters is relatively small ($\sim$0.1% of the total protein content [25]). Thus, characteristic changes in PrP marker bands of FT-IR spectra from S samples may well be obscured by alterations in relative protein content and composition during the pathological process that are of much greater magnitude. These alterations certainly include the up-regulation of several genes [21] and more or less controlled catabolic activities in the diseased organ. Furthermore, the PrP^{Sc} accumulation in the cerebellum of scrapie 263K-infected hamsters occurs in diffuse and granular structures rather than in the quite large classical congophilic plaques, as is the case for other TSEs or Alzheimer's disease.

Spatially resolved analysis of protein IR absorption in N and S samples revealed that the protein-associated molecular changes detectable in the amide I and amide II regions of the IR spectrum are not equally distributed over the investigated layers of the cerebellum. While differences in protein absorption between normal and infected samples were visible in the granular layer and in axonal regions of the neurons, they did not occur in stratum moleculare (2) (Fig. 4). As stratum moleculare consists of only a few neurons and mainly of dendrites emerging from stratum ganglionare, the majority of protein alterations seem to occur in the cells of stratum granulosum and in perikarya and axons of Purkinje cells.

Future experiments will concentrate on the enhancement of the S/N ratio using signal averaging and increased detector sensitivities to systematically apply FT-IR difference spectroscopic techniques. In addition, an ultrabright IR synchrotron radiation source at the Berlin BESSY II storage ring will help to attain significantly increased sensitivities and a higher spatial resolution for investigations of single nerve cells [12,26].

4.2. Diagnostic potential of FT-IR spectroscopy

Because of the BSE epidemic in Great Britain and the emergence of a new variant of CJD an automated test for TSEs that allows simple and rapid screening of large sample numbers is urgently needed. Our study revealed a consistent link between scrapie infection and a number of molecular changes which can be detected by FT-IR spectroscopy in situ without prior staining or labeling. It is possible to acquire IR spectra from homogenized samples and perform cluster analysis within a few minutes. The scrapie-associated spectral markers observed in FT-IR spectra from infected brains can be analyzed reliably by non-subjective mathematical methods. Cluster analysis clearly separated infected from uninfected tissue (Fig. 6) and might therefore provide a new post-mortem diagnostic tool for the detection of scrapie and related diseases.

The next steps for the development of a rapid FT-IR detection method for TSEs will include the examination of samples from animals in preclinical stages of the disease and from individuals with non-TSE-like disorders as well as the use of more sophisticated data evaluation techniques for the construction of a reference database. In addition to the brain tissue analyzed in this study, other components of the central and peripheral nervous system, such as dorsal root ganglia and cerebrospinal fluid, will be probed in future studies.

Acknowledgements

We would like to thank Angelika Brauer who performed IR measurements on the homogenized tissue samples.

References

[1] H. Diringer, M. Beekes, U. Oberdieck, The nature of the

scrapie agent: the virus theory, Ann. NY Acad. Sci. 724 (1994) 246–258.
[2] S.B. Prusiner, M.R. Scott, S.J. DeArmond, F.E. Cohen, Prion protein biology, Cell 93 (1998) 337–348.
[3] H.H. Mantsch, D. Chapman (Eds.), Infrared Spectroscopy of Biomolecules, Wiley-Liss, New York, 1996.
[4] D. Naumann, D. Helm, H. Labischinski, Microbiological characterizations by FT- spectroscopy, Nature 351 (1991) 81–82.
[5] J. Wang, M. Sowa, H.H. Mantsch, A. Bittner, H.M. Heise, Comparison of different infrared measurement techniques in the clinical analysis of biofluids, Trends Anal. Chem. 15 (1996) 286–295.
[6] M. Diem, S. Boydston-White, L. Chiriboga, Infrared spectroscopy of cells and tissues: shining light onto a novel subject, Appl. Spectrosc. 53 (1999) 148A–161A.
[7] M. Jackson, M.G. Sowa, H.H. Mantsch, Infrared spectroscopy: a new frontier in medicine, Biophys. Chem. 68 (1997) 109–125.
[8] S.M. LeVine, D.L.B. Wetzel, Analysis of brain tissue by FT-IR microspectroscopy, Appl. Spectrosc. 28 (1993) 385–412.
[9] P. Lasch, D. Naumann, FT-IR microspectroscopic imaging of human carcinoma thin sections based on pattern recognition techniques, Cell Mol. Biol. 44 (1998) 189–202.
[10] L.-P. Choo, M. Jackson, W.C. Halliday, H.H. Mantsch, Infrared spectroscopic characterization of multiple sclerosis plaques in the human central nervous system, Biochim. Biophys. Acta 1182 (1993) 333–337.
[11] L.H. Kidder, V.F. Kalasinsky, J.L. Luke, I.W. Levin, E.N. Lewis, Visualization of silicone gel in human breast tissue using new infrared imaging spectroscopy, Nature Med. 3 (1997) 235–237.
[12] L.-P. Choo, D.L.B. Wetzel, W.C. Halliday, M. Jackson, S.M. LeVine, H.H. Mantsch, In situ characterization of β-amyloid in Alzheimer's diseased tissue by Synchrotron Fourier transform infrared microspectroscopy, Biophys. J. 71 (1996) 1672–1679.
[13] D. Helm, H. Labischinski, G. Schallehn, D. Naumann, Classification and identification of bacteria by Fourier-transform infrared spectroscopy, J. Gen. Microbiol. 137 (1991) 69–79.
[14] H.L. Casal, H.H. Mantsch, Polymorphic phase behavior of phospholipid membranes, Biochim. Biophys. Acta 779 (1984) 381–401.
[15] F. Siebert, Infrared spectroscopy applied to biochemical and biological problems, Methods Enzymol. 246 (1995) 501–526.
[16] J. Liquier, R. Taillandier, Infrared spectroscopy of nucleic acids, in: H.H. Mantsch, D. Chapman (Eds.), Infrared Spectroscopy of Biological Molecules, Wiley-Liss, New York, 1996, pp. 131–158.
[17] R.V. Krstic, Human Microscopic Anatomy: An Atlas for Students of Medicine and Biology, Springer-Verlag, Berlin, 1991.
[18] Z. Guan, M. Soderberg, P. Sindelar, S.B. Prusiner, K. Kristensson, G. Dallner, Lipid composition in scrapie-infected mouse brain: Prion infection increases the levels of dolichyl phosphate and ubiquinone, J. Neurochem. 66 (1996) 277–285.
[19] C. Schultz, D. Naumann, In vivo study of the state of order of the membranes of Gram-negative bacteria by Fourier-transform infrared spectroscopy (FT-IR), FEBS Lett. 294 (1991) 43–46.
[20] D.J. Moore, R. Mendelsohn, Adaptation to altered growth temperatures in *Acholeplasma laidlawii* B: Fourier transform infrared studies of acyl chain conformational order in live cells, Biochemistry 33 (1994) 4080–4085.
[21] J.F. Diedrich, R.I. Carp, A.T. Haase, Increased expression of heat shock protein, transferrin, and β-microglobulin in astrocytes during scrapie, Microb. Pathog. 15 (1993) 1–6.
[22] P. Lasch, C.P. Schultz, D. Naumann, The influence of poly-(L-lysine) and porin on the domain structure of mixed vesicles composed of lipopolysaccharide and phospholipid an infrared spectroscopic study, Biophys. J. 75 (1998) 840–852.
[23] J.J. Chen, B.P. Yu, Alterations in mitochondrial membrane fluidity by lipid peroxidation products, Free Radic. Biol. Med. 17 (1994) 411–418.
[24] K.M. Pan, M. Baldwin, J. Nguyen, M. Gasset, A. Serban, D. Groth, I. Mehlhorn, Z. Huang, R.J. Fletterick, F.E. Cohen, S.B. Prusiner, Conversion of alpha-helices into beta-sheets features in the formation of the scrapie prion proteins, Proc. Natl. Acad. Sci. USA 90 (1993) 10962–10966.
[25] M. Beekes, E. Baldauf, S. Caßens, H. Diringer, P. Keyes, A.C. Scott, G.A.H. Wells, P. Brown, C.J. Gibbs Jr., D.C. Gajdusek, Western blot mapping of disease-specific amyloid in various animal species and humans with TSEs using a high-yield purification method, J. Gen. Virol. 76 (1995) 2567–2576.
[26] N. Jamin, P. Dumas, J. Moncuit, W.-H. Fridman, J.-L. Teillaud, G.L. Carr, G.P. Williams, Highly resolved chemical imaging of living cells by using synchrotron infrared microspectrometry, Proc. Natl. Acad. Sci. USA 95 (1998) 4837–4840.